Applied Physics Letters

Efficiency improvement analysis of nano-patterned sapphire substrates and semi-transparent superlattice contact layer in UVC light-emitting diodes

Cite as: Appl. Phys. Lett. **117**, 261102 (2020); https://doi.org/10.1063/5.0037588
Submitted: 14 November 2020 • Accepted: 14 December 2020 • Published Online: 29 December 2020

Chia-Yen Huang, Chia-Lung Tsai, Cheng-Yao Huang, et al.

Efficiency improvement analysis of nano-patterned sapphire substrates and semi-transparent superlattice contact layer in UVC light-emitting diodes

Cite as: Appl. Phys. Lett. **117**, 261102 (2020); doi: 10.1063/5.0037588
Submitted: 14 November 2020 · Accepted: 14 December 2020 ·
Published Online: 29 December 2020

View Online Export Citation CrossMark

Chia-Yen Huang,[1,a)] Chia-Lung Tsai,[1] Cheng-Yao Huang,[2] Rong-Yu Yang,[3] YewChung Sermon Wu,[4] Hung-Wei Yen,[2] and Yi-Keng Fu[1]

AFFILIATIONS

[1]Electronic and Optoelectronic System Research Laboratories, Industrial Technology Research Institute, 195, Sec. 4, Chung Hsing Rd., Hsinchu, Taiwan
[2]Department of Materials Science and Engineering, National Taiwan University, No. 1, Sec. 4, Roosevelt Rd., Taipei, Taiwan
[3]Department of Materials Science and Engineering, National Chung-Hsing University, 145 Xingda Rd., Taichung, Taiwan
[4]Department of Materials Science and Engineering, National Chiao-Tung University, 1001 Ta Hsueh Rd., Hsinchu, Taiwan

[a)]Author to whom correspondence should be addressed: itriA70432@itri.org.tw

ABSTRACT

UVC light-emitting diodes (LEDs, $\lambda = 275$ nm) with different types of contact layers and sapphire substrates were demonstrated on high-quality AlN templates. For LEDs on flat sapphire substrates (FSSs), replacing the absorbing p-GaN contact with p-AlGaN short-period superlattices (p-SPSLs) strongly enhanced the emission along the substrate normal. The integrated external quantum efficiency (EQE) increased from 2.4% to 3.9% under I = 350 mA. For LEDs with a p-SPSL contact, replacing the FSS with nano-patterned sapphire substrates slightly deteriorated the quality of epitaxy, but the overall EQE is still enhanced to 4.4% under I > 350 mA without lens encapsulation. According to the far-field intensity measurement, the light extraction is better improved along the high emission angle to the substrate normal. The interplay among substrates, dipole polarization, and EQE enhancement factors was further analyzed and discussed in the context.

UVC irradiation ($\lambda = 200$ nm–280 nm) is an effective measure for disinfection and sterilization for all pathogens by triggering the deformation of its DNA or RNA. AlGaN-based UVC light-emitting diodes (LEDs) possess many advantages such as compact size, fast turn-on, and non-toxicity compared to conventional deep-UV light sources.[1,2] Therefore, UVC LEDs have attracted much attention for consumer-based disinfection applications especially during the COVID-19 pandemic. However, the limited output power still hampers its replacement in high-volume or large-area wafer/air purification. Although an external quantum efficiency (EQE) of more than 10% was once reported by Takano *et al.*,[3] the state-of-the-art EQE was presented only at a low current injection level. For high-power applications, a decent EQE at a high current injection level is much desirable. In UVC LEDs, two major factors have limited the overall EQE: the high threading dislocation density (TDD) in the epitaxy for the low internal quantum efficiency (IQE) and the band edge absorption of the p-type GaN contact layer for the low light-extraction efficiency (LEE). The TDD of the AlN template directly grown by conventional metal-organic chemical vapor deposition (MOCVD) was usually $>5 \times 10^9\ \mathrm{cm}^{-2}$.[4] According to Ban *et al.*, the IQE under low excess carrier density ($\sim 10^{18}\ \mathrm{cm}^{-3}$) is less than 20% if TDD $> 1 \times 10^9\ \mathrm{cm}^{-2}$.[5] Although the TDD of bulk AlN substrates could be extremely low,[6,7] the cost effectiveness of AlN substrates for commercial UVC LEDs is difficult to justify. Therefore, improving the quality of AlN on sapphire substrates is still the focus of technology advances. Novel epitaxial techniques such as pulse-feeding of precursors and growth parameter modulation were developed.[8–11] For example, Bai *et al.* varied the V/III ratio, and Demir *et al.* varied the growth temperature during single AlN growth. The frequent growth parameter changes aimed to balance between the crystal quality and surface morphologies. Another popular approach is introduction of voids to the AlN template by either utilizing nano-patterned sapphire substrates (NPSSs) or epitaxial overgrowth over pre-patterned AlN templates.[12–17] Because the TD propagation stops at the surface of voids, the TDD is significantly reduced after the film coalesces. The full-width at half-maximum (FWHM) of the x-ray rocking curve (XRC) measurement on 10–12 reflection of AlN on the NPSS was reported as low as 200–250 arcsec. However, the short diffusion length of Al adatoms inevitably hindered the coalescence of the AlN film. Direct growth of AlN on the NPSS suffered from a relatively thick (>5 μm) AlN template. From the perspective of uniformity and warpage management, a further reduced thickness is desirable for scalability. Recently, Miyake *et al.* have demonstrated ~300 nm-thin AlN buffers with XRCs for 10–12 FWHM less than 300 arcsec by high-temperature annealing (HTA).[18,19] Various groups also verified the high-quality AlN and UVC-LED regrowth on these HTA-AlN buffers.[20–26] In InGaN-based UV-visible LEDs, utilizing patterned sapphire substrates (PSSs) favored both IQE and LEE. However, whether and how much the NPSS favors the EQE of UVC LEDs were rarely discussed experimentally. Some theoretical simulation suggested that the utilization of the NPSS in AlGaN-based UVC LEDs does not necessarily improve the LEE due to the absorbing contact layers.[16,27] Unfortunately, realizing UVC LEDs with a transparent p-AlGaN contact and NPSS encountered many practical difficulties. First, the hole density in p-AlGaN was much lower because of its high ionization energy. Devices with a p-AlGaN contact layer all demonstrated a drastic increase in forward voltage.[3,28,29] Second, if the LED epitaxial quality on NPSS is not good enough, a better light-extraction efficiency (LEE) could be still compromised due to the poorer hole injection or the deteriorated IQE. To overcome these issues, we grew the UVC LED on high-quality AlN buffer on the NPSS as the starting point. The compressive strain in the template is managed by a high Si-doping in the regrown AlN layer.[25] We also replaced the p-GaN contact layer with a p-AlGaN short-period superlattice (p-SPSL) for its improved carrier transport properties.[29,30] In this study, we demonstrated a 275 nm UVC LED with a p-SPSL contact layer on a high-quality and void-free AlN template on the NPSS. The same LED structure was also grown on flat sapphire substrates (FSSs) with either p-GaN or p-SPSL contact layers as references. Finally, we achieved an EQE of 4.4% under I > 350 mA before lens encapsulation.

Figure 1(a) illustrates the fabrication process of the void-free AlN template on the NPSS. SiO_2 hardmask was deposited on a 2-in. c-plane FSS for nano-imprinting lithography.[31] The patterned hardmask consisted of 500-nm-wide quasi-periodic nano-holes. We chose this pattern arrangement simply because of the mold availability. The patterns were formed by wet etching.[32] The final pattern is around 560 nm in width and 180 nm in depth. Figure 1(b) shows the 5 μm × 5 μm atomic force microscope (AFM) images of the fresh NPSS after hardmask removal. A high-quality AlN template was deposited on the NPSS by SCIOCS Ltd. with hydride vapor phase epitaxy (HVPE).[33] The surface is preliminarily flattened by HVPE and then completely flattened after a 3.5 μm Si-doped AlN regrowth in our TNSC SR-4000 MOCVD system. The Si-doped AlN was grown at T = 1240 °C and P = 10 kPa without any interruption or growth parameter changes. The [Si] is 2×10^{19} cm^{-3} according to the secondary ion mass spectroscopy measurement. The high Si-doping relaxed the inherent compressive strain from the HVPE buffer.[25] Figures 1(c) and 1(d) show the example of the AFM image of the HVPE buffer layer and the Si-doped AlN template on the NPSS, respectively. The final AlN is atomically flat between the discrete macro-steps on the surface. Above UVC LEDs, the epilayer consisted of a 150 nm compositionally graded layer, a 1650 nm n-$Al_{0.65}Ga_{0.35}N$, four pairs of AlGaN MQW, 40 nm p-$Al_{0.75}Ga_{0.25}N$ electron blocking layers (EBLs), and an 80 nm p-SPSL contact layer at top. The p-SPSL contact layer is composed of 32 pairs of alternating $Al_{0.6}Ga_{0.4}N$ and $Al_{0.35}Ga_{0.65}N$ layers with the same thickness. N-AlGaN was grown at T = 1060 °C and P = 35 kPa, and the [Si] is 2.5×10^{19} cm^{-3}. The AFM image of the final LED surface is shown in Fig. 1(e). As references, the same

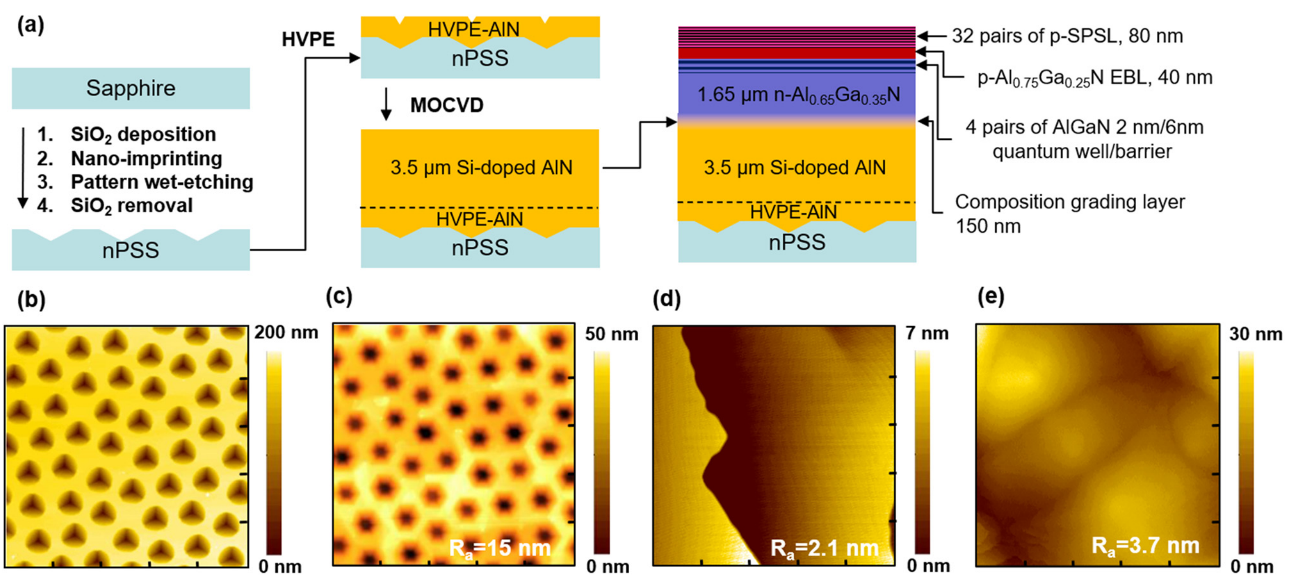

FIG. 1. (a) Schematic process flow of void-less UVC-LEDs on the NPSS. 5 μm × 5μm AFM image of (b) fresh NPSS, (c) HVPE buffer, (d) Si-doped AlN, and (e) final LED surface. The roughness (R_a) of Figs. 1(c)–1(e) is labeled in the corner.

HVPE and MOCVD processes were conducted on FSSs as well. The p-contact layer of the FSS LED was either 80 nm bulk p-GaN or the same aforementioned p-SPSL. For brevity, we noted the LED with a p-SPSL contact on the NPSS as NPSS-LED-S, the LED with a p-SPSL contact on the FSS as FSS-LED-S, and the LED with a bulk p-GaN contact on the FSS as FSS-LED-B.

The epilayer quality and its strain state were assessed by x-ray diffraction. XRCs on 0002 and 10–12 reflection evaluated the quality of HVPE buffer, Si-doped AlN, and n-AlGaN. Since FSS-LED-S and FSS-LED-B possessed the same underlayer, we only present one of them. The 0002 and 10–12 XRCs of Si-doped AlN (FSS-AlN:Si or NPSS-AlN:Si) and n-AlGaN (FSS-AlGaN or NPSS-AlGaN) are plotted in Figs. 2(a) and 2(b), respectively. Figure 2(c) plots the 0002 ω-2θ scans of AlN layers in both FSS-LEDs and NPSS-LEDs. The XRC FWHM evolution from HVPE buffer to n-AlGaN is summarized in Fig. 2(d). In either FSS-LEDs or NPSS-LEDs, the 10–12 FWHMs were broader than the 0002 FWHMs. According to the mosaic model,[34] most of the threading dislocations (TDs) possessed an edge component. In the FSS-LED, the 10–12 FWHMs remained around 250 arcsec during growth. In comparison, 10–12 FWHM in nPSS LEDs was 373 arc sec in HVPE buffer, reduced to 205 arcsec after the regrowth of Si-doped AlN, and then increased to 384 arcsec in n-AlGaN. According to the same model, the final TDD of n-AlGaN on the FSS and NPSS was estimated to be $5.0 \times 10^8\ \mathrm{cm}^{-2}$ and $1.3 \times 10^9\ \mathrm{cm}^{-2}$, respectively.

To explain the evolution of 10–12 FWHMs, we need to extract the in-plane strain (ε_x) states of HVPE AlN buffer and Si-doped AlN from 0002 ω-2θ scans. In FSS LEDs, AlN is more compressive in the buffer ($\varepsilon_x = -0.265\%$) and then gradually relaxed to a nearly free-standing state ($\varepsilon_x = -0.014\%$) after AlN:Si regrowth. In NPSS-LEDs, the final template Si-doped AlN is more compressive. The final ε_x of AlN is -0.144%, which is 0.13% more compressive than that of FSS-LEDs. Take the unstrained in-plane lattice constant a = 3.111 Å for AlN, a = 3.189 Å for GaN, and a = 3.138 Å for $Al_{0.65}Ga_{0.35}N$ by Vegard's Law. The initial strain seen by n-AlGaN is -0.88% and -1.01% on the FSS and NPSS, respectively. The strain of a thick compressive film could be relaxed by tilting or bending (1) preexisting dislocations or (2) newly nucleated dislocations. If the compressive film

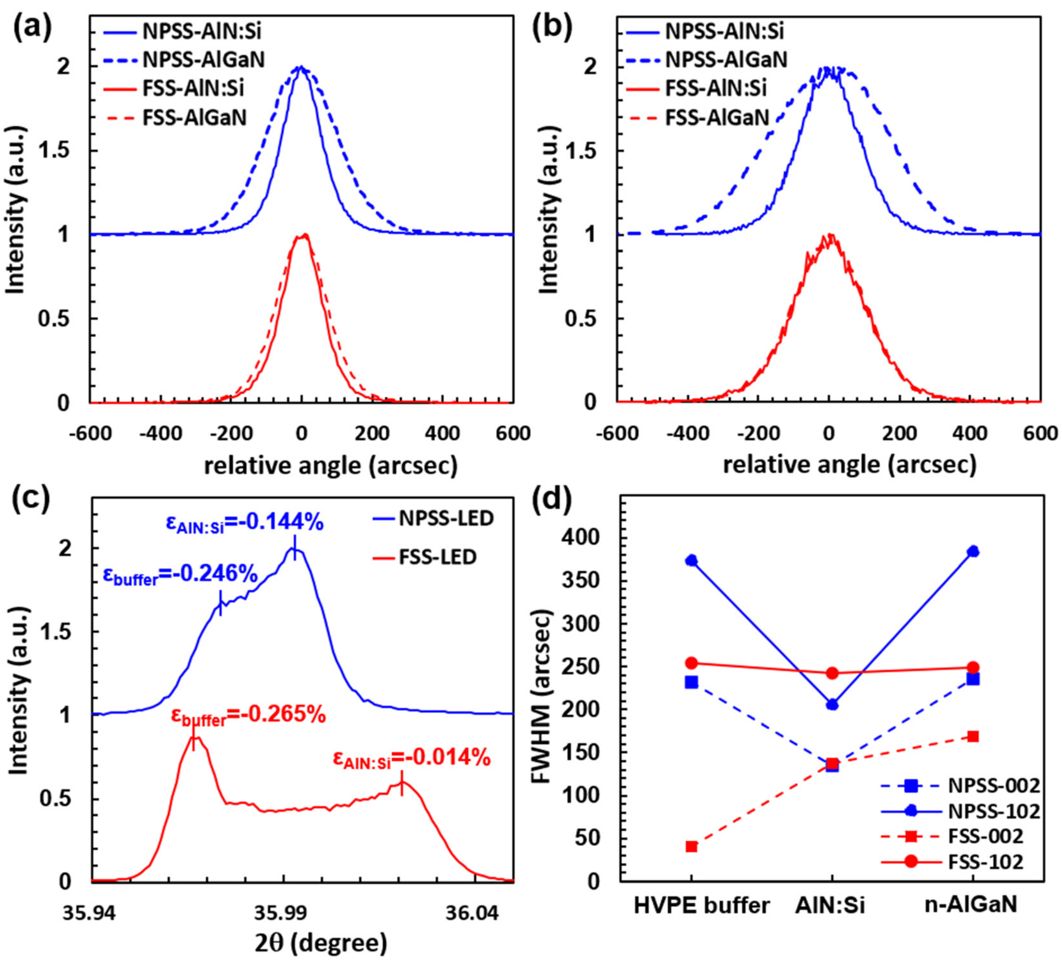

FIG. 2. X-ray rocking curves of Si-doped AlN (solid line) and the n-AlGaN layer (dashed line) on (a) 0002 and (b)10–12 reflection. (c)0002 ω-2θ scan of AlN templates in FSS-LEDs (blue) and NPSS-LEDs (red). XRCs and ω-2θ scans were normalized and vertically shifted for clarity. (d) 0002 and 10–12 XRC FWHM evolution from HVPE buffer to n-AlGaN.

can be stabilized by the preexisting TDs, the overall TDD will remain at the same level after growth. This explained the consistent 10–12 XRC FWHMs in the LED epitaxy on the FSS. However, if the strain energy is higher, or the preexisting TD is too few, just like the case of the n-AlGaN on NPSS, nucleation of new dislocations could be triggered, and then the crystal quality starts to deteriorate. The much lowered 10–12 FWHM of Si-doped AlN on the NPSS suggested that TD annihilation took place in the early stage. Fewer TDs contributed to the strain relaxation during the growth of Si-doped AlN, and so the final strain remained more compressive. How TDs effectively annihilate in the void-less AlN template requires further investigation. It is worth noticing that n-AlGaN quality deterioration was attributed to the TDD and the strain state of the AlN template, not to the NPSS. In our experiences (not shown here), growing the same n-AlGaN on FSS-AlN with a similar TDD level and compressive strain state was not stable neither. Improving the IQE by further reducing the TDD of the AlN template is challenging on either the FSS or the NPSS. Therefore, we shall directly optimize the n-AlGaN structure on the NPSS to improve the IQE and LEE simultaneously.

Transmission electron microscopy images of NPSS-LED-S are shown in Figs. 3(a)–3(e). Figure 3(b) clearly demonstrates the existence of the short-period superlattices. AlN above the patterns appeared to be void-free in Figs. 3(a) and 3(e). Figures 3(c) and 3(d) show the inclined threading dislocations within n-AlGaN and Si-doped AlN, respectively. However, their formation mechanisms are different. TD inclination in Si-doped AlN originated from the Al vacancy compensation. When vacancies interacted with the edge dislocation cores in AlN, the extra planes in the epitaxy gradually recede and dislocations incline. TD inclination in n-AlGaN is driven by the lattice mismatch between AlGaN and AlN. As the compressive n-AlGaN grew thick, it could not retain pseudomorphic on the AlN template. Evidence of the partial relaxation in micrometer-thick n-AlGaN can also be found in Ref. 25.

The epi-wafers were fabricated into 1.14 mm × 1.14 mm flip chips. The p-metal was Ni/Au, and the n-metal was Ti/Al/Ni/Au metal multilayers. Selected LED chips were bonded on a ceramic sub-mount for testing without encapsulation. Output power was measured in an integrated sphere with pulsed current injection up to 500 mA. Coloaded FSS-LED-B and FSS-LED-S wafers were backside-polished for the transmittance measurement. The transmittance spectra were normalized to its maximum transmittance in the long wavelength region. The EQE curves were then calculated and are plotted in Fig. 4(a). At I = 350 mA, the EQE increased from 2.4% to 3.8% after replacing the p-GaN contact with p-SPSLs. The significant efficiency improvement is apparently due to the reduced absorption from the p-contact layer. Figure 4(b) plots the electroluminescence (EL) under I = 350 mA (solid line) and the normalized transmittance spectrum (dashed line) of both FSS-LEDs with bulk p-GaN (in black) and p-SPSLs (in red). At $\lambda = 275$ nm, the transmittance in FSS-LED-B was only 3%, while that in FSS-LED-S was around 70%. The final EQE of NPSS-LED-S was 4.4%, which was 14.8% higher than that of NPSS-LED-S. From Fig. 2, we can tell that the n-AlGaN quality on the NPSS template was not as good as that on the FSS template, which explained the lower EQE of NPSS-LED-S under I < 50 mA. From another perspective, we experimentally confirmed that the EQE enhancement of NPSS-LED-S under high current injection is attributed to the improved LEE. In terms of wall-plug efficiency (WPE), the forward voltage (V_f) needs to be taken into account. The V_f values of FSS-LED-B, FSS-LED-S, and NPSS-LED-S under I = 350 mA were 6.7 V, 10.4 V, and 10.5 V, and the WPE was estimated to be 1.6%, 1.6%, and 1.9%, respectively. The improvement in WPE is rather insignificant

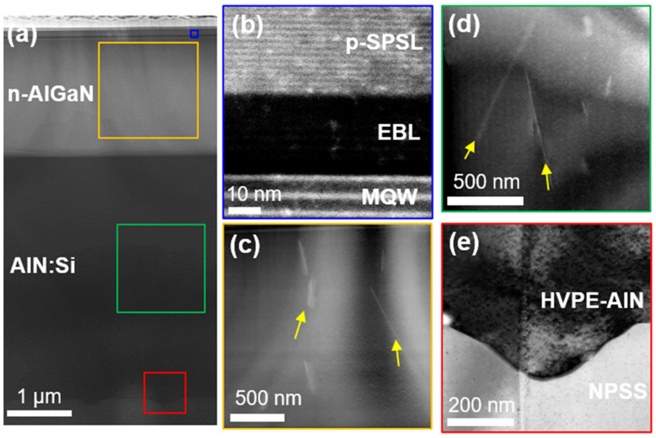

FIG. 3. (a) Cross-sectional HAADF TEM images of NPSS-LED-S with magnified STEM images near (b) active region, (c) n-AlGaN, (d) Si-doped AlN, and (e) NPSS. Yellow arrows in (c) and (d) mark inclined dislocations in n-AlGaN and Si-doped AlN.

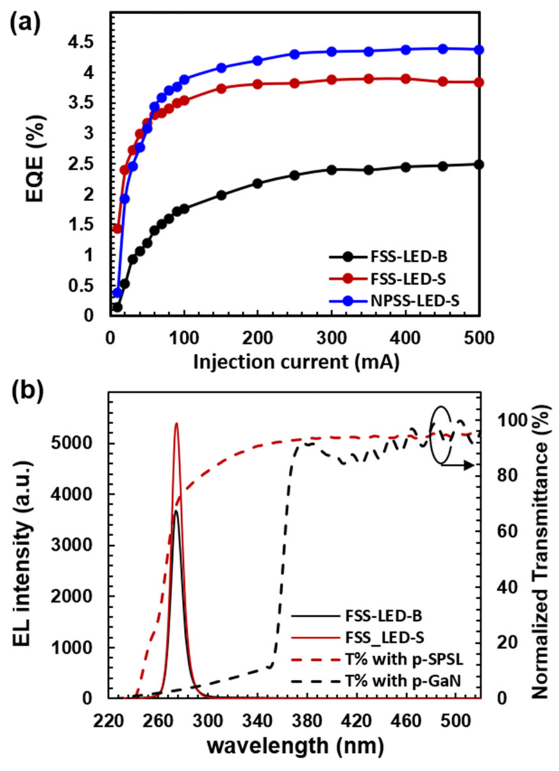

FIG. 4. (a) The EQE curves of three LEDs up to I = 500 mA. (b) The electroluminescence spectrum under I = 350 mA (solid lines to left axis) and the normalized transmittance spectrum (dashed line to right axis) of the FSS-LEDs with a p-GaN (black) or p-SPSL (red) contact layer.

due to the higher V_f values with p-SPSLs. Nevertheless, the V_f values were still lower than those of other reported UVC-LEDs with p-AlGaN contact layers,[3,29] which is explained by the tunneling-assisted hole injection in p-SPSLs.[30] It is worth noticing that three samples underwent the same chip processing, which was originally optimized for the p-GaN contact. Further WPE improvement might be achieved with more structure and processing optimization with p-SPSLs.

In comparison with the EQE benchmarks from the study by Takano *et al.*[3] and Shatalov *et al.*,[11] there seems to be a gap for the peak EQE values. Therefore, it is worth comparing our approaches with available information. Both Shatalov *et al.* and we used the p-AlGaN contact layer with Ni/Au metal for FSS-LEDs. Shatalov *et al.* achieved a lower TDD ($\sim 2.0 \times 10^8\,\mathrm{cm}^{-2}$) than ours by growing a very thick AlN. Therefore, their high EQE at a low current injection level in bare die (7.5% at I = 20 mA) was attributed to the superior IQE. However, the EQE dropped significantly with current injection. The EQE reduced to be less than 5% when I = 100 mA, while our EQE was at the same high level up to I = 500 mA. Therefore, our approach has higher potential for a high-power point source. As mentioned in the previous paragraph, the strain management of n-AlGaN is critical if the initial TDD is very low. If Shatlov *et al.* adopted a relatively thin n-AlGaN thickness to retain the low TDD, the device would suffer from heating or current crowding under high current injection. This might explain the different trend between EQE curves. The state-of-the-art EQE performance by T. Takano *et al.* is a combination of multiple LEE enhancement approaches. In our study, we did not have access to the highly reflective Rh p-metal and the UVC-transparent resin. To compare the EQE in a similar platform, we referred their earlier demonstration of UVC LEDs with p-AlGaN and Ni/Au contacts on the FSS.[35] The peak EQE in bare die was also around 4%, which is very close to that in our FSS-LEDs. Therefore, EQE of our LEDs might also boost multiple folds after applying similar LEE enhancement design. Besides, our Al composition in n-AlGaN (Al = 65%) is much lower than theirs (Al = 77%). Our approach with a pre-relaxed Si-doped AlN template also showed stronger potential for a lower sheet resistance and n-contact resistance.

To further analyze the LEE improvement from the p-SPSL and NPSS, an angle-resolved far-field measurement was conducted for all LEDs. To minimize the influence from the n-AlGaN quality difference, the injection current was chosen to be 350 mA. The emission angle (θ) is defined by the angle between the substrate normal and the light axis. A polarizer was mounted before the detector to extract the transverse-electric (TE) and transverse-magnetic (TM) field intensity, $I_{TE/TM}(\theta)$. The measurement and data-analysis methodology could be found in Ref. 36. The $I_{TE/TM}(\theta)$ values before and after normalization are plotted in Figs. 5(a) and 5(b). The angular-dependent power enhancement factor of TE-polarized emission, $f_{TE}(\theta)$, is defined by the intensity ratio of selected LEDs by

$$f_{TE,SPSL}(\theta) = \frac{I_{TE,FSS-LED-S}(\theta)}{I_{TE,FSS-LED-B}(\theta)}, \quad (1)$$

$$f_{TE,NPSS}(\theta) = \frac{I_{TE,NPSS-LED-S}(\theta)}{I_{TE,FSS-LED-S}(\theta)}. \quad (2)$$

The same definition also applied to $f_{TM}(\theta)$ values. Therefore, $f_{TE/TM,SPSL}$ represents the angular power enhancement by the p-contact replacement with the same FSS. $f_{TE/TM,NPSS}$ represents the enhancement by the NPSS with the same p-SPSL contact. All $f(\theta)$ values are summarized in Fig. 5(c). $I_{TE}(\theta)$ was strongest along $\theta = 0°$ and gradually diminished as θ increased. The same trend applied to $f_{TE,SPSL}$. The θ-dependence of $f_{TE,SPSL}$ suggested that the limited contact transparency dominated the enhancement. Because photons along high θ travel longer in the semi-transparent p-SPSL layers before being reflected, the light extraction enhancement from the p-side becomes less effective. Since f_{TE} was stronger along low θ values, the emission pattern became narrower after normalization. On the other hand, $f_{TE,NPSS}$ varied oppositely with θ. The $f_{TE,NPSS}$ value was around 1.1 near $\theta = 0°$ and slowly increased to ~ 1.25 as θ approached 90°. Since the power enhancement originates from the additional scattering at the AlN/sapphire interface, photons traveling along θ with a higher reflectivity naturally benefit more. The TM-polarized light possessed a wing-like emission pattern. $I_{TM}(\theta)$ reached its local maximum when $\theta = 60$–$65°$ and approached zero when $\theta < 15$ degree. The trend of angle dependence of f_{TM} values was similar to that of the f_{TE} values except for $f_{TM,NPSS}$ at $\theta < 30°$. The normalized $I_{TM}(\theta)$ was also squeezed toward low θ values due to the higher f_{TM} values at low θ values. Since the TM field was very weak at low θ values, few photons scattered from higher θ values could yield a prominent enhancement.

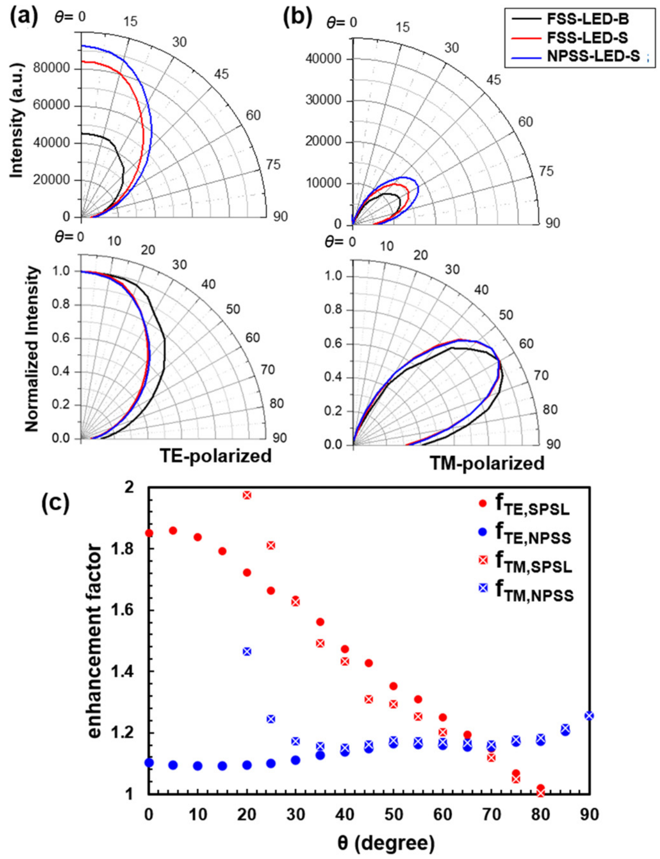

FIG. 5. The far-field emission intensity distribution before (upper) and after (lower) normalization of three LEDs with (a) TE-polarized and (b) TM-polarized emission. (c) The emission angle dependence of power enhancement factors by p-SPSL replacement or NPSS utilization.

It is also possible that the deviating f_{TM} values at low θ values are due to the background noises.

In summary, we revealed challenges and opportunities for improving the UVC LED efficiency by p-contact and substrate replacement. First, the superior AlN template quality on the NPSS does not necessarily yield a better quality in n-AlGaN. We attributed the difficulty to the narrowed n-AlGaN design window for strain management. If the misfit strain of n-AlGaN could be further suppressed, the good quality of the AlN template shall be better transferred to the LED epitaxy. Second, the efficiency enhancement from contact replacement and NPSS utilization possessed an opposite angular dependence, but the trends were similar between TE- and TM-polarized light. Improving the contact transparency favors the low-angle emission, while NPSS favors the high-angle emission. For UVC LEDs, which are dominated by TE-polarized emission, improving the contact layer transparency is more essential for power enhancement. On the other hand, if the original field intensity is stronger along a high emission angle, for example, TM-polarized emission, improvement by NPSS utilization will be more effective.

The authors thank SCIOCS Ltd., Japan, for their generous support in HVPE AlN deposition service. The authors also acknowledge Dr. Yuh-Renn Wu of National Taiwan University for the insightful discussion.

DATA AVAILABILITY

The data that support the findings of this study are available from the corresponding author upon reasonable request.

REFERENCES

[1] M. Kneissl and J. Rass, "III-Nitride ultraviolet emitters," in *Springer Series in Materials Science* (Springer, 2016).
[2] D. K. Kim and D. H. Kang, Appl. Environ. Microbiol. **84**, e00944-18 (2018).
[3] T. Takano, T. Mino, J. Sakai, N. Noguchi, K. Tsubaki, and H. Hirayama, Appl. Phys. Express **10**, 031002 (2017).
[4] J. Mickevicius, G. Tamulaitis, M. Shur, M. Shatalov, J. Yang, and R. Gaska, Appl. Phys. Lett. **101**, 211902 (2012).
[5] K. Ban, J. Yamamoto, K. Takeda, K. Ide, M. Iwaya, T. Takeuchi, S. Kamiyama, I. Akasaki, and H. Amano, Appl. Phys. Express **4**, 052101 (2011).
[6] Z. Bryan, I. Bryan, J. Xie, S. Mita, Z. Sitar, and R. Collazo, Appl. Phys. Lett. **106**, 142107 (2015).
[7] Y. Kumagai, Y. Kubota, T. Nagashima, T. Kinoshita, R. Dalmau, R. Schlesser, B. Moody, J. Xie, H. Murakami, A. Koukitu, and Z. Sitar, Appl. Phys. Express **5**, 055504 (2012).
[8] J. Bai, M. Dudley, W. H. Sun, H. M. Wang, and M. A. Khan, Appl. Phys. Lett. **88**, 051903 (2006).
[9] H. Hirayama, Appl. Phys. Lett. **91**, 071901 (2007).
[10] I. Demir, H. Li, Y. Robin, R. McClintock, S. Elagoz, and M. Razeghi, J. Phys. D: Appl. Phys. **51**, 085104 (2018).
[11] M. Shatalov, W. Sun, A. Lunev, X. Hu, A. Dobrinsky, Y. Bilenko, J. Yang, M. Shur, R. Gaska, C. Moe, G. Garrett, and M. Wraback, Appl. Phys. Express **5**, 082101 (2012).
[12] R. Jain, W. Sun, J. Yang, M. Shatalov, X. Hu, A. Sattu, A. Lunev, J. Deng, I. Shturm, Y. Bilenko, R. Gaska, and M. S. Shur, Appl. Phys. Lett. **93**, 051113 (2008).
[13] P. Dong, J. Yan, J. Wang, Y. Zhang, C. Geng, T. Wei, P. Cong, Y. Zhang, J. Zeng, Y. Tian, L. Sun, Q. Yan, J. Li, S. Fan, and Z. Qin, Appl. Phys. Lett. **102**, 241113 (2013).
[14] R. Ni, X. Chen, J. Yan, L. Zhang, Y. Guo, J. Wang, J. Li, and Y. Zhang, J. Alloys Compd. **777**, 344 (2019).
[15] B. Tang, H. Hu, H. Wan, J. Zhao, L. Gong, Y. Lei, Q. Zhao, and S. Zhou, Appl. Sur. Sci. **518**, 146218 (2020).
[16] S. Hagedorn, S. Walde, N. Susilo, C. Netzel, N. Tillner, R. Unger, P. Manley, E. Ziffer, T. Wernicke, C. Becker, H. J. Lugauer, M. Kneissl, and M. Weyers, Phys. Status Solidi A **217**, 1900796 (2020).
[17] S. Xiao, N. Jiang, K. Shojiki, K. Uesugi, and H. Miyake, Jpn. J Appl. Phys., Part 1 **58**, SC1003 (2019).
[18] H. Miyake, C.-H. Lin, K. Tokoro, and K. Hiramatsu, J. Cryst. Growth **456**, 155 (2016).
[19] R. Yoshizawa, H. Miyake, and K. Hiramatsu, J. Jpn. Appl. Phys., Part 1 **57**, 01AD05 (2018).
[20] C. Y. Huang, P. Y. Wu, K. S. Chang, Y. H. Lin, W. C. Peng, Y. Y. Chang, J. P. Li, H. W. Yen, Y. C. Sermon, H. M. Wu, and H. C. Kuo, AIP Adv. **7**, 055110 (2017).
[21] S. Walde, S. Hagedorn, and M. Weyers, J. Jpn. Appl. Phys., Part 1 **58**, SC1002 (2019).
[22] N. Susilo, S. Hagedorn, D. Jaeger, H. Miyake, U. Zeimer, C. Reich, B. Neuschuz, L. Sulmoni, M. Guttmann, F. Mehnke, C. Kuhn, T. Wernicke, M. Weyers, and M. Kneiss, Appl. Phys. Lett. **112**, 041110 (2018).
[23] Y. Itokazu, S. Kuwaba, M. Jo, N. Kamata, and H. Hirayama, J. Jpn. Appl. Phys., Part 1 **58**, SC1056 (2019).
[24] R. Ni, C. C. Chuo, K. Yang, Y. Ai, L. Zhang, Z. Cheng, Z. Liu, L. Jia, and Y. Zhang, J. Alloys Compd. **794**, 8 (2019).
[25] C. Y. Huang, S. Walde, C. L. Tsai, C. Netzel, H. H. Liu, S. Hagedorn, Y. R. Wu, Y. K. Fu, and M. Weyers, J. Jpn. Appl. Phys., Part 1 **59**, 070904 (2020).
[26] Y. Iba, K. Shojiki, K. Uesugi, S. Xiao, and H. Miyake, J. Cryst. Growth **532**, 125397 (2020).
[27] Y. K. Ooi and J. Zhang, IEEE Photonics J. **10**, 1 (2018).
[28] N. Maeda and H. Hirayama, Phys. Status Solidi C **10**, 1521 (2013).
[29] M. Martens, C. Kuhn, E. Ziffer, T. Simoneit, V. Kueller, A. Knauer, J. Rass, T. Wernicke, S. Einfeldt, M. Weyers, and M. Kneissl, Appl. Phys. Lett. **108**, 151108 (2016).
[30] X. Chen, K. Y. Ho, and Y. R. Wu, Opt. Express **23**, 32367 (2015).
[31] H. W. Huang, C. H. Lin, C. C. Yu, B. D. Lee, C. H. Chiu, C. F. Lai, H. C. Kuo, K. M. Leung, T. C. Lu, and S. C. Wang, Semicond. Sci. Technol. **23**, 045022 (2008).
[32] Y. C. Sermon Wu, A. P. S. Isabel, J. H. Zheng, B. W. Lin, J. H. Li, and C. C. Lin, Materials **8**, 1993 (2015).
[33] H. Fujikura, T. Konno, T. Kimura, and H. Miyake, Appl. Phys. Express **13**, 025506 (2020).
[34] S. R. Lee, A. M. West, A. A. Allerman, K. E. Waldrip, D. M. Follstaedt, P. P. Provencio, D. D. Koleske, and C. R. Abernathy, Appl. Phys. Lett. **86**, 241904 (2005).
[35] H. Hirayama, N. Maeda, S. Fujikawa, S. Toyoda, and N. Kamata, Jpn. J. Appl. Phys., Part 1 **53**, 100209 (2014).
[36] X. Chen, C. Ji, Y. Xiang, X. Kang, B. Shen, and T. Yu, Opt. Express **24**, A935 (2016).